

# Electrospun BiFeO<sub>3</sub> Nanofibers for Vibrational Energy Harvesting Application

Arun Ichangi, Khan Lê, Albert Queraltó, Matthias Grosch, René Weißing, Feray Ünlü, Amadi Kingsley Chijioke, Anjneya Verma, Thomas Fischer, Roman Surmenev, and Sanjay Mathur\*

Bismuth ferrite (BiFeO<sub>3</sub>, BFO) has found application in a wide range of fields owing to its fascinating multiferroic properties. Herein, the interplay between the piezoelectric properties and morphology of BFO nanostructures is exploited for vibrational energy harvesting application by tailoring BFO to a high aspect ratio and high surface area nanofiber morphology. This work demonstrates a facile pathway for the fabrication of high-performance flexible nanogenerators, based on BFO nanofibers, from a cost-effective and energy-efficient electrospinning technique. The X-ray diffraction data of calcined fibers confirm the formation of noncentrosymmetric crystalline perovskite phase. The morphological characterization by scanning electron microscopy shows a compact anisotropic nanofibrous morphology. For the fabrication of nanogenerators, BFO nanofibers are embedded in a piezoactive polymer matrix (polyvinylidene fluoride [PVDF]). As-fabricated BFO/PVDF composite nanogenerators produce a high peak-to-peak voltage output of 7.6 V, with an average output power density of  $185 \pm 106 \text{ nW cm}^{-2}$  upon periodic application of force through finger knocking.

to the development of piezoelectric nanogenerators (PENGs).<sup>[2–4]</sup> The field of mechanical energy harvesting using PENGs has gained significant attention in recent years<sup>[5–9]</sup> mainly attributed to high voltages that can be generated from compact PENGs, which carry the promise of autonomous powering of low power and mobile systems like sensors and wearable electronics.<sup>[10–12]</sup> Recent advances in the fabrication of composite PENGs with nanofiller materials in the form of piezoelectric nanoparticles, nanorods, nanofibers (NFs), and nanowires have shown that high-power outputs can be realized.<sup>[13–17]</sup> Of these, electrospun piezoelectric nanofiber (PNF)-based PENGs present an interesting case for achieving high output voltage owing to their high surface area and high aspect ratio intrinsic to their anisotropic morphologies. Additionally, electrospinning

## 1. Introduction


The dire need for alternative energy sources to reduce the reliance on fossil fuels has brought renewable energy sources like solar, wind, and geothermal<sup>[1]</sup> into the focus of research. While these sources are most suited for large-scale energy production, the need for compact and mobile power sources has led

to the development of piezoelectric nanogenerators (PENGs).<sup>[2–4]</sup> The field of mechanical energy harvesting using PENGs has gained significant attention in recent years<sup>[5–9]</sup> mainly attributed to high voltages that can be generated from compact PENGs, which carry the promise of autonomous powering of low power and mobile systems like sensors and wearable electronics.<sup>[10–12]</sup> Recent advances in the fabrication of composite PENGs with nanofiller materials in the form of piezoelectric nanoparticles, nanorods, nanofibers (NFs), and nanowires have shown that high-power outputs can be realized.<sup>[13–17]</sup> Of these, electrospun piezoelectric nanofiber (PNF)-based PENGs present an interesting case for achieving high output voltage owing to their high surface area and high aspect ratio intrinsic to their anisotropic morphologies. Additionally, electrospinning is a less energy-intensive process that makes it a cost-effective alternative. The electrospinning technique inevitably leads to polycrystalline PNFs; therefore, for any meaningful use of PNFs in PENG application, the PNFs must be ferroelectric. PENGs based on lead zirconate titanate (PZT) PNFs have been widely reported owing to their high piezoelectric coefficients.<sup>[18–21]</sup> However, due to the toxicity of lead-based materials there has been a pressing need to replace them with environmentally benign and biocompatible materials.

Bismuth ferrite (BiFeO<sub>3</sub>, BFO) has been widely studied as an alternative lead-free piezoelectric material, which also exhibits interesting photovoltaic, photocatalytic, magnetic, and multiferroic properties.<sup>[22–27]</sup> For a photovoltaic device, BFO NFs were fabricated by laterally aligning them on interdigital electrodes. The resulting photocurrent from the ferroelectric-photovoltaic effect of BFO NFs was found to be much higher than for BFO thin films alone.<sup>[22]</sup> Despite many reports on various properties of BFO NFs, the work on exploiting the piezoelectric properties of BFO NFs through PENG fabrication is lacking. We previously reported on the synthesis of electrospun BFO NFs and studies of their piezoelectric properties ( $d_{33}$  coefficient: 11 pC/N) using a direct piezoelectric force microscopy (DPFM) technique.<sup>[23]</sup> Even though the reported  $d_{33}$  for BFO NFs was lower than for thin films, a theoretical study on BFO showed that it has a large ferroelectric polarization of  $90 \mu\text{C cm}^{-2}$  along [111] direction.<sup>[24]</sup> In one study, a PENG

A. Ichangi, K. Lê, M. Grosch, R. Weißing, F. Ünlü, A. K. Chijioke, A. Verma, T. Fischer, R. Surmenev, S. Mathur  
Institute of Inorganic Chemistry  
University of Cologne  
Greinstr. 6, 50939 Cologne, Germany  
E-mail: sanjay.mathur@uni-koeln.de

A. Queraltó  
Superconducting Materials and Large-scale nanostructures Department  
Institut de Ciència de Materials de Barcelona (ICMAB-CSIC)  
Campus UAB, 08193 Bellaterra, Spain

 The ORCID identification number(s) for the author(s) of this article can be found under <https://doi.org/10.1002/adem.202101394>.

© 2021 The Authors. Advanced Engineering Materials published by Wiley-VCH GmbH. This is an open access article under the terms of the Creative Commons Attribution-NonCommercial License, which permits use, distribution and reproduction in any medium, provided the original work is properly cited and is not used for commercial purposes.

DOI: 10.1002/adem.202101394

fabricated by embedding BFO nanoparticles in PDMS matrix was able to generate a voltage of  $\approx 3$  V and a short-circuit current of 250 nA under periodic application of stress through hand pressing.<sup>[25]</sup>

We report here a flexible PENG based on electrospun BFO PNFs embedded in poly(vinylidene fluoride) (PVDF) polymer matrix fabricated by a sol-gel-based electrospinning technique, which offers the flexibility to tune the composition and morphology of materials. The PENG was able to produce a high peak-to-peak ( $V_{p-p}$ ) output voltage of 7.6 V under a periodic application of force through finger knocking.

## 2. Experimental Section

### 2.1. Material Synthesis

$\text{BiFeO}_3$  NFs (BFO NFs) were prepared by using bismuth (III)-nitrate pentahydrate ( $\text{Bi}(\text{NO}_3)_3 \cdot 5\text{H}_2\text{O}$ , Sigma-Aldrich) and iron(III)-nitrate nonahydrate ( $\text{Fe}(\text{NO}_3)_3 \cdot 9\text{H}_2\text{O}$ , Sigma-Aldrich) salts. In a typical synthesis, a stoichiometric ratio (0.002 mol) of salts was stirred in 0.2 mL of glacial acetic acid. A polymer solution was prepared by dissolving 600 mg of polyacrylonitrile (PAN,  $M_w = 150\,000$ , Sigma-Aldrich) in 10 mL of *N,N*-dimethylformamide (DMF) solution. Following this step, the polymer solution was added drop by drop to the salt solution and stirred overnight to form a sol that was loaded onto a syringe and electrospun with experimental parameters listed in **Table 1**.

The resulting NF meshes were calcined at  $500^\circ\text{C}$  for 3 h with a ramp of  $1^\circ\text{C min}^{-1}$  to yield crystalline  $\text{BiFeO}_3$  as a single-phase material. PENGs were fabricated by dispersing BFO PNFs in PVDF (Sigma-Aldrich,  $M_w \approx 534\,000\text{ g mol}^{-1}$ ) matrix. In this study, three sets of PENGs with varying mass fractions of BFO—1 wt% (BFO-1), 3 wt% (BFO-3), and 5 wt% (BFO-5)—were fabricated and studied. Mass fractions beyond 5 wt% were not considered to avoid agglomeration of BFO, which usually occurs at higher concentrations.<sup>[26]</sup> Proportionate amount of BFO PNFs were first weighed in a 20 mL beaker; later 20 wt% of PVDF polymer was added followed by 2 mL DMF (Fisher Chemical, 99.5%) solvent. The resulting mixture was stirred at 600 rpm at  $50^\circ\text{C}$  for 7 h to homogeneously disperse the BFO NFs in PVDF polymer matrix. Afterward, the reaction mixture was transferred to an oven at  $80^\circ\text{C}$  and dried for 17 h to ensure the removal of any remaining trace amount of DMF solvent. The resulting PENG was then cut into  $2 \times 2$  cm sizes and sputtered with 20 nm of Au on an area of  $1.5 \times 1.5$  cm on either side, which were then connected to copper lead wires of the oscilloscope (Tektronix TDS 210) to record the generated output voltage and current.

**Table 1.** Electrospinning conditions for the fabrication of  $\text{BiFeO}_3$  NFs.

Syringe volume	6 mL
Needle	21 gauge, inner $\varnothing$ 0.514 mm
Feed rate	$5\ \mu\text{L min}^{-1}$
Voltage applied	1.5 kV cm
Distance (syringe tip to collector plate)	10 cm
Rotation speed of collector drum	100 rpm

All the fabricated PENGs were tested at room temperature ( $\approx 20$ – $25^\circ\text{C}$ ).

### 2.2. Material Characterization

The crystalline structure and phase purity of the BFO PNFs were recorded by X-ray diffractometry (XRD) (STOE-Stadi MP, Mo Ka source) at room temperature. The morphology of the calcined BFO PNFs was investigated using a scanning electron microscope (SEM) (FEI NanoSEM 430) and a high-resolution transmission electron microscope (HR-TEM) (JEOL JEM-2200 FS) operated at accelerating voltage of 200 kV. Raman spectra were recorded at room temperature using a 532 nm laser with 1 mW power (Renishaw  $\mu$ Raman spectrometer with a Renishaw Centrus 05TJ52 detector). Fourier-transform-infrared (FTIR) spectra were recorded using a PerkinElmer Spectrum 400 FTIR spectrometer. Thermogravimetric (TG) measurement was performed using TG/DSC1 (Mettler Toledo GmbH, Germany) apparatus under air with a ramp of  $10^\circ\text{C min}^{-1}$ .

## 3. Results and Discussion

To analyze the evolution of the BFO perovskite phase, the decomposition and the subsequent crystallization behavior of the as-spun NFs were studied by TG measurement, as shown in **Figure 1c**. The electrospun NFs showed a multistep decomposition behavior corresponding to an initial weight loss of 1.6% occurring at a temperature of  $\approx 90^\circ\text{C}$  possibly due to the release of adsorbed water from the NFs. This is followed by a second weight loss of  $\approx 7.8\%$  occurring in the temperature range of  $\approx 110$ – $185^\circ\text{C}$  and corresponding to the removal of residual glacial acetic acid (boiling point:  $118^\circ\text{C}$ ) and DMF solvent (boiling point:  $153^\circ\text{C}$ ). The subsequent weight loss of  $\approx 6.44\%$  at  $\approx 226^\circ\text{C}$  corresponded to the decomposition of nitrate species. The final step accompanied with a weight loss of  $\approx 19.3\%$  in the temperature range  $\approx 230$ – $420^\circ\text{C}$  was attributed to decomposition and removal of organic polymer. No further weight loss was observed even at higher temperatures that confirmed the formation of stable material with a definite composition (BFO).

The XRD pattern showed a polycrystalline phase of the calcined PNFs with a predominance of the (110) peak, suggesting a preferred grain growth direction. The average crystallite size of BFO PNFs was estimated to be 149.37 nm using the Scherrer Equation (1).

$$D = \frac{k\lambda}{B \cos \theta} \quad (1)$$

where  $D$  is the crystallite size,  $\lambda$  is the wavelength of the X-ray radiation source (Mo source,  $0.7107\ \text{\AA}$ ),  $B$  is the full width at the half maximum (FWHM),  $k$  is a constant whose value is 0.89, and  $\theta$  is the angle of diffraction of the most intense peak, in this case (110) reflex.

Rietveld refinement was performed on the XRD pattern of calcined BFO NFs using MAUD software program to determine the unit cell structure and symmetry.<sup>[27–29]</sup> **Figure 2a** shows a very good fit between the experimental XRD and the calculated profile, with final fitting parameters of  $R_{wp} = 3.617\%$ ,  $R_b = 2.750\%$ ,

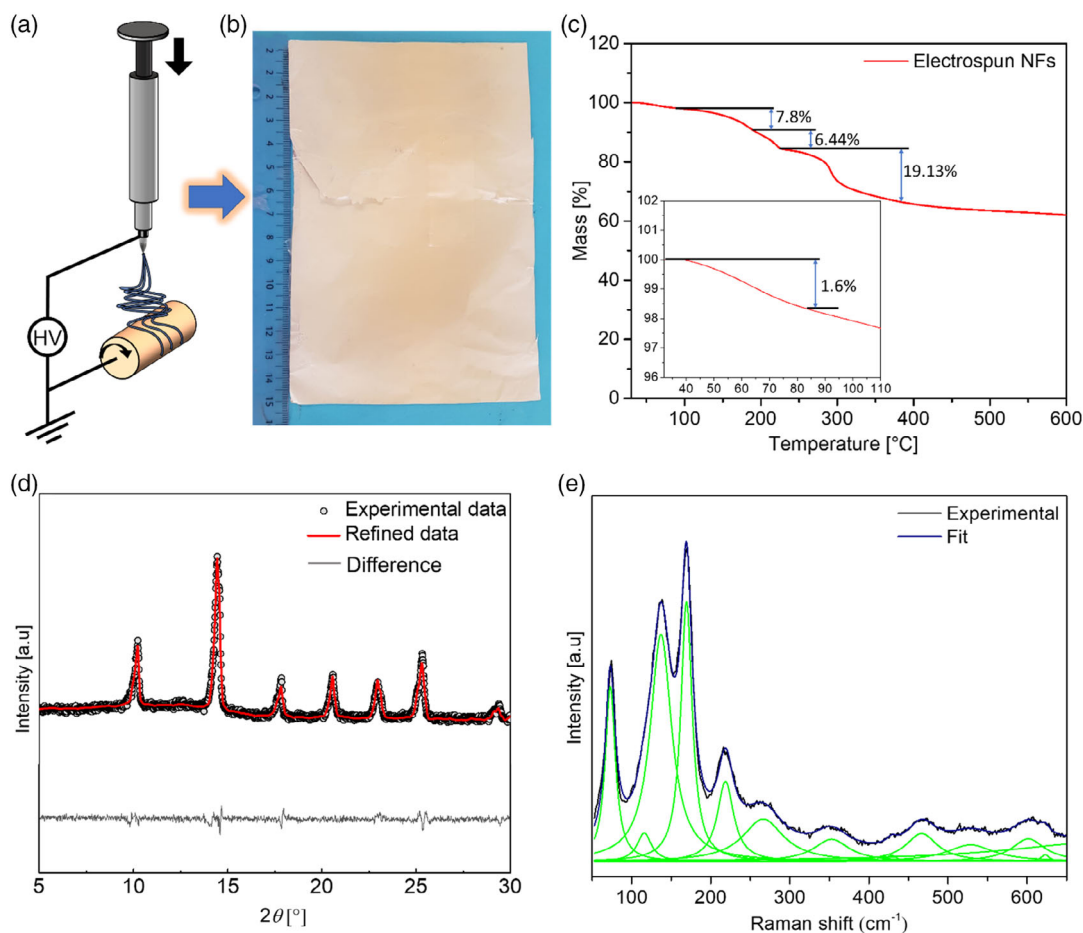


**Figure 1.** a) Schematic representation of the electrospinning process used for the fabrication of BFO fiber meshes; b) image of electrospun BFO NFs collected on aluminum foil and c) TG profile showing the decomposition behavior of electrospun NFs; d) Rietveld refinement of XRD pattern of BFO PNFs calcined at 500 °C for 3 h; e) Raman spectra of BFO PNFs with Lorentzian function peak fitting.

and  $\text{sig} = 0.192$ . The lattice constants, estimated from the refinement, were  $a = 5.58569 \text{ \AA}$  and  $c = 13.86077 \text{ \AA}$ , confirmed a noncentrosymmetric rhombohedral structure with a  $R3c$  space group. Thus, the calcined PNFs were both piezoelectric and ferroelectric. Moreover, Raman spectroscopy was performed on BFO PNFs to investigate the chemical structure. As described in the literature, rhombohedral structure of BFO with a  $R3c$  symmetry has in total 13 Raman active modes, composed of 4  $A_1$  optical acoustic modes and 9  $E$  modes.<sup>[30]</sup> Figure 2b shows the Raman spectra of BFO PNFs fitted with Lorentzian functions and the different Raman active modes listed in Table 2.

The modes  $E-1$ ,  $A_1-1$ ,  $A_1-2$ ,  $A_1-3$ ,  $E-4$ ,  $E-6$ ,  $E-7$ , and  $E-9$  match with reported modes of BFO nanostructures.<sup>[31]</sup>  $E-2$ ,  $A_1-4$ , and  $E-8$  are slightly shifted, which may be due to the different processing conditions of BFO PNFs. The piezoelectric properties are known to depend on the morphology of nanostructures;<sup>[32,33]</sup> therefore, the morphology of PNFs was investigated in detail by SEM and TEM imaging. The morphology of the as-electrospun NFs showed an average diameter of  $331 \pm 100 \text{ nm}$  (Figure 2c), while Figure 2d shows that the calcined NFs at 500 °C were found to agglomerate leading to thicker diameters with an average size of  $747 \pm 219 \text{ nm}$ .

The diameter of an individual strand of PNF was estimated from TEM image, as shown in Figure 2e, as a structurally compact individual PNF with a diameter of about 150 nm. The diameter of the individual PNF shrunk considerably from  $331 \pm 100$  to  $\approx 150 \text{ nm}$  upon calcination due to the decomposition of the organic polymer and subsequent densification leading to a pure BFO phase. Figure 2f shows a HR-TEM image taken at the edge of the PNF showing the lattice fringes with an interplanar distance of 0.279 nm, which is in good agreement with the distance of (110) plane obtained from Rietveld refinement.

It has been reported in the literature that the most common semicrystalline chain conformations of PVDF polymer are of four different kinds: the alternate trans and gauche ( $TG^+$   $TG^-$ ) chain conformation is  $\alpha$  and  $\delta$  phase,  $T_3G^+ T_3G^-$  chain conformation is  $\gamma$  phase, and all trans (TTTT)  $\beta$  phase.<sup>[34,35]</sup> Of these phases, the electroactive phases  $\gamma$  and  $\beta$  have attracted a lot of attention due to their relatively high piezoelectric coefficient.<sup>[36,37]</sup> Previous reports have shown that certain nanofillers influence the phase formation in PVDF.<sup>[38,39]</sup> To understand the influence of BFO NFs on the phase evolution of PVDF, FTIR spectra were recorded on the PENGs as shown in Figure 2b. The exclusive peaks of electroactive  $\beta$  and  $\gamma$  phase

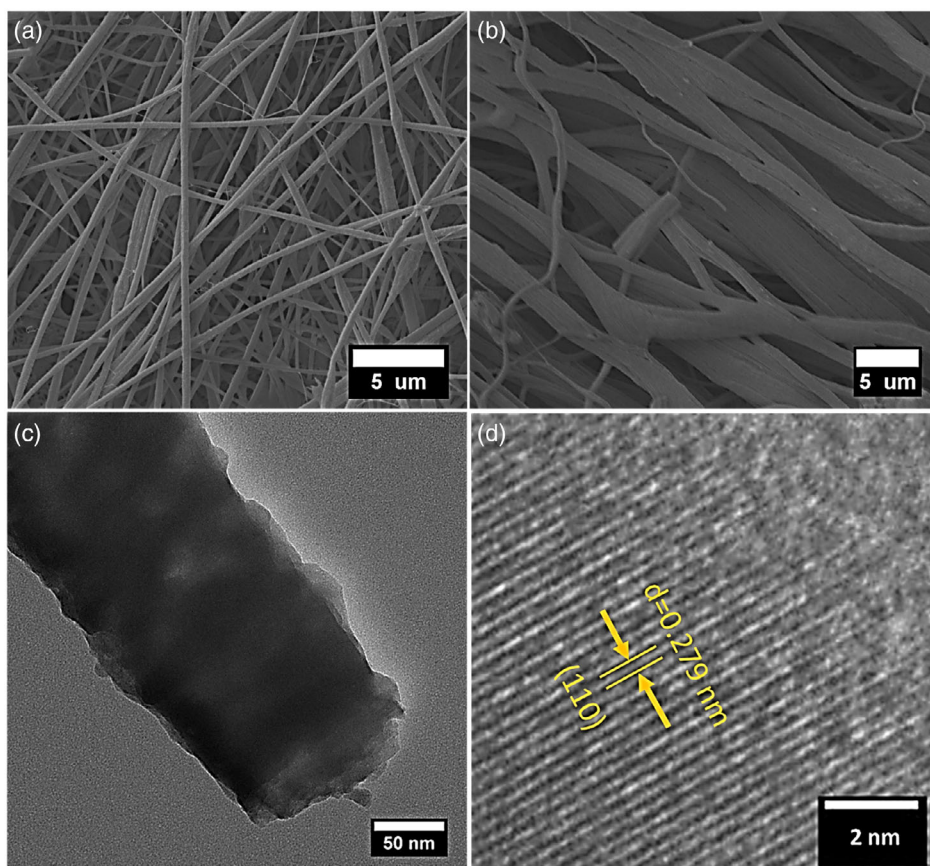


**Figure 2.** a,b) SEM images of as-electrospun and calcined BFO PNFs; c,d) TEM image of an individual PNF and HR-TEM image showing lattice fringes of BFO PNF.

**Table 2.** Peak positions of Raman active modes of BFO PNFs.

Mode	E-1	E-2	A <sub>1</sub> -1	A <sub>1</sub> -2	A <sub>1</sub> -3	E-4	E-6	A <sub>1</sub> -4	E-7	E-8	E-9
Position [cm <sup>-1</sup> ]	72.95	115.88	136.99	169.31	218.59	266.23	352.71	428.84	466.65	528	601.64

can be seen in the IR spectra at 1275 cm<sup>-1</sup> (orange line) and 1232 cm<sup>-1</sup> (black line), respectively, which is in good agreement with the literature.<sup>[40,41]</sup> Using the literature values, the other characteristic peaks at 511 and 840 cm<sup>-1</sup> which appears as a shoulder (Figure S1, Supporting Information) were assigned to the  $\beta$  phase.<sup>[42]</sup> The characteristic peaks of the  $\gamma$  phase can be seen at 431, 480, 812, 833, 1232, and 1429 cm<sup>-1</sup>. Interestingly, the exclusive peak for the nonelectroactive  $\alpha$  phase, which appears at 763 cm<sup>-1</sup>, is relatively weak. This might indicate that the PENGs that were deposited were already highly electroactive. To estimate the amount of total electroactive phase in the fabricated PENGs, Equation (2), reported in literature, was used.<sup>[40]</sup>

$$F(\text{EA}) = \frac{I_{\text{EA}}}{1.26I_{763} + I_{\text{EA}}} \quad (2)$$

where  $I_{763}$  and  $I_{\text{EA}}$  are the intensity of absorbance of peaks at 763 and 840 cm<sup>-1</sup>, respectively. The factor of 1.26 is derived by dividing

the absorbance coefficient of the  $\beta$  phase with that of  $\alpha$  phase, which are  $7.7 \times 10^4$  and  $6.1 \times 10^4$  cm<sup>2</sup> mol<sup>-1</sup>, respectively. Using the above equation, the electroactive phase fraction for pristine PVDF, BFO-1, BFO-3, and BFO-5 was estimated to be 78%, 75%, 70%, and 73%, respectively (Figure 3).

#### 4. Characterization of PENG

The performance of PENGs with different mass fractions of BFO PNFs embedded in PVDF matrix was studied with respect to the open-circuit voltage ( $V_{\text{oc}}$ ) and short-circuit current ( $I_{\text{sc}}$ ) generated by the PENG under vertical periodic knocking with a finger on its surface. The PENG was clamped at one end and the other end was left free for vibrations, as shown in Figure 4. When a certain force is applied on the surface of the PENG, an instantaneous potential difference is generated across the thickness of PENG resulting from the piezoelectric property of BFO PNFs. This

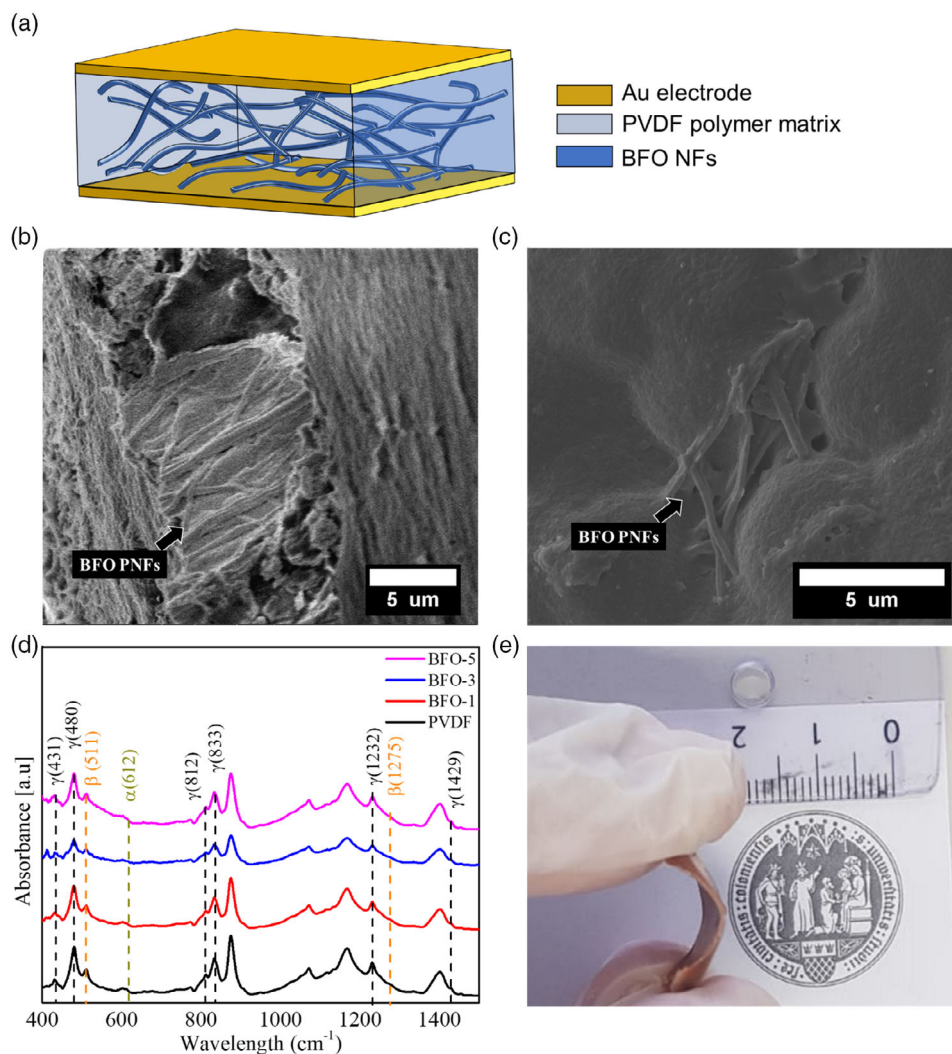


**Figure 3.** a) Schematic of PENG, b) top-view SEM image showing spatially aligned BFO PNFs protruding out of the side face of a PENG, c) top view of the surface of the PENG showing embedded BFO PNFs, d) FTIR spectra of the fabricated PENGs, with the dashed lines marking the characteristic modes of  $\alpha$  and  $\beta$  phase, and e) image showing a flexible PENG.

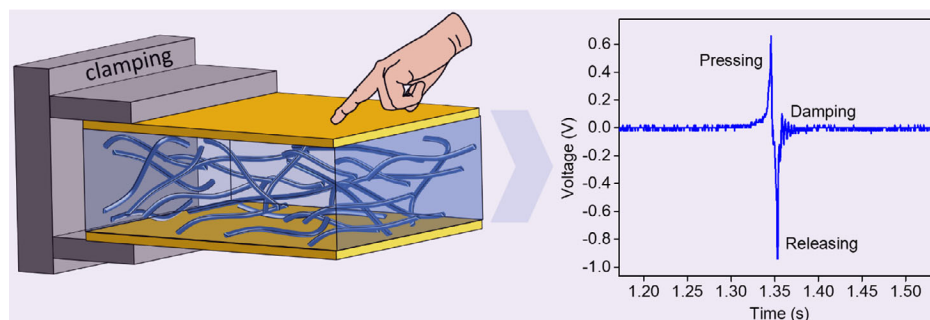


**Figure 4.** Schematic of the clamped PENG (left) and the voltage response of the PENG upon finger knocking (right).

potential difference causes the flow of electrons in an external circuit. Upon withdrawal of the finger applying the force, the PENG relaxes in the opposite direction resulting in an opposite polarity and flow of generated charges, as shown in Figure 4.

All the fabricated PENGs were tested without any additional poling process. The respective output voltages generated by the PENGs with different mass fraction of BFO PNFs are shown in **Figure 5a**. PENGs with BFO PNFs showed much greater

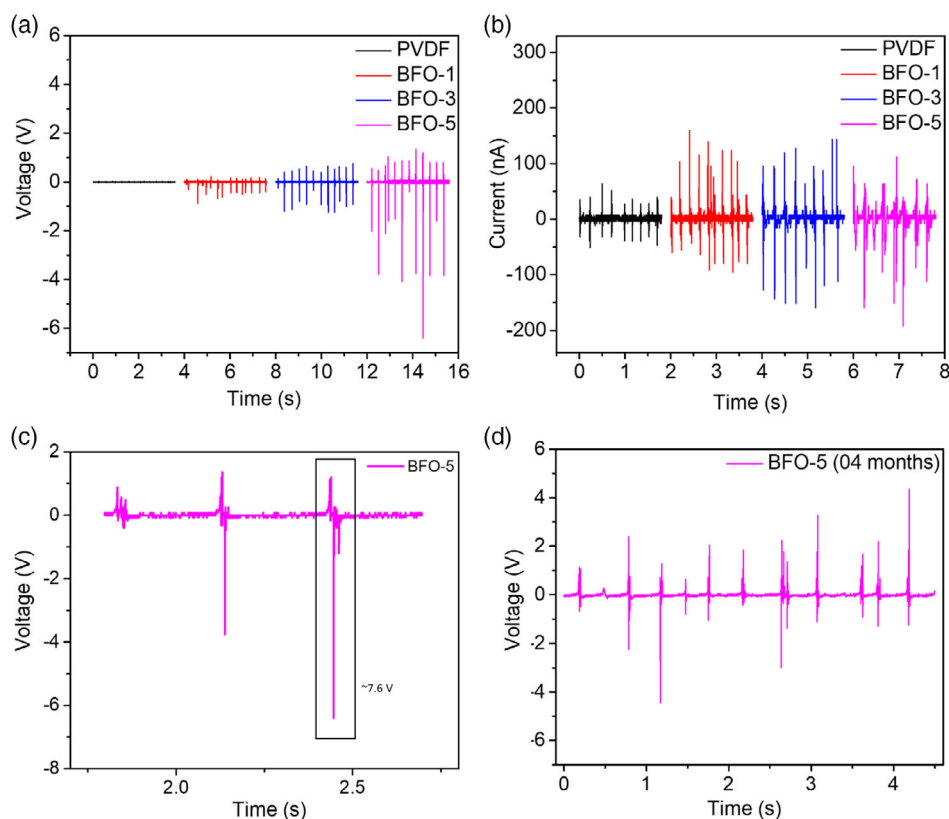


**Figure 5.** a) Open-circuit voltage response of the pristine PVDF (black), BFO-1 (red), BFO-3 (blue), and BFO-5 (magenta); b) measured short-circuit current ( $I_{sc}$ ) of PENGs in an external circuit; c) open-circuit voltage of BFO-5 PENG showing a high  $V_{p-p}$  of 7.6 V. Finger tapping leads to variations in the recorded output voltages ( $V_{p-p}$ ) of the PENG due to the irregularities in forces, speeds, impacted area, etc.; d) open-circuit voltage response of BFO-5 PENG measured after 4 months of storage.

**Table 3.** Average voltage and current from the fabricated PENG with different wt% of BFO PNFs embedded in PVDF matrix.

Sample	$V_{oc}$ [V]	$I_{sc}$ [nA]	Power density [nW]
PVDF	$0.030 \pm 0.004$	$38.66 \pm 7.48$	$1.16 \pm 0.27$
BFO-1	$0.490 \pm 0.167$	$72.80 \pm 16.41$	$35.67 \pm 14.57$
BFO-3	$1.030 \pm 0.175$	$132.00 \pm 24.56$	$135.96 \pm 34.25$
BFO-5	$3.140 \pm 1.514$	$133.33 \pm 41.00$	$418.65 \pm 239.42$

voltage response than pure PVDF film. Moreover, the voltage output increases with increasing mass fraction of BFO PNFs confirming that the embedded BFO PNFs contribute to higher voltage response of the PENG. The average  $V_{oc}$  increases from 0.03 V (Figure S2, Supporting Information) to  $3.14 \pm 1.514$  V, for mass fraction from 0 to 5 wt%, under a certain knocking force. **Table 3** shows the average  $V_{oc}$ ,  $I_{sc}$ , and power output generated by the fabricated PENGs.

It is noteworthy that the average  $V_{oc}$  recorded from the BFO-5 PENG is comparable to the previously reported 3 V that was generated by embedding 40 wt% of BFO nanoparticles in PDMS matrix.<sup>[25]</sup> The main reasons for such high output voltage with

a significant lower mass fraction of electrospun BFO PNFs (5 wt%) as compared to BFO nanoparticles (40 wt%) are due to the high aspect ratio, high surface area, and spatial alignment of the PNFs in the PVDF matrix. The high aspect ratio ensures that the imparted force on the surface of the PENG induces a long range piezoelectric potential difference across the entire length of the embedded PNFs, and the high surface area aids in more efficient charge extraction from the surface. The spatial alignment of the PNFs augments the piezoelectric and voltage output of the PENGs, which was observed previously in similar systems.<sup>[17,43]</sup> The average output voltage recorded for BFO-1 and BFO-3 was at  $0.490 \pm 0.167$  and  $1.030 \pm 0.175$  V, respectively.

To determine the power generated by the PENGs, the short-circuit current was measured by connecting a 1 M $\Omega$  resistor in series. The respective currents from the PENGs are shown in Figure 5b. The total output power of the BFO-5 PENG was found to be  $418.65 \pm 239.42$  nW, which is significantly higher than the power density of pristine PVDF PENG. Moreover, the PENG BFO-5 yielded a very high peak-to-peak ( $V_{p-p}$ ) voltage of 7.6 V (Figure 5c), which, to the best of our knowledge, is the highest recorded for electrospun BFO PNFs. From Table 3, it can be deduced that the addition of BFO PNFs to the polymer matrix enhanced the effect on the power output as compared to

**Table 4.** Comparison of PENGs based on lead-free perovskite oxide materials.

Nanogenerator	Output voltage [ $V_{oc}$ ]	$V_{p-p}$	Output power [ $\mu W$ ]	Reference
Mn-doped (K,Na) NbO <sub>3</sub> MFs/PDMS	$\approx 0.3$	–	$\approx 0.015$	[44]
(K,Na) NbO <sub>3</sub> NFs/PDMS	1.6	–	–	[45]
BaTiO <sub>3</sub> NFs (vertically aligned)/PDMS	$2.67 \pm 0.11$	–	$0.1840 \pm 0.0233$	[17]
BaTiO <sub>3</sub> NFs (randomly aligned)/PDMS	$0.56 \pm 0.04$	–	$0.0086 \pm 0.0023$	[17]
BaTiO <sub>3</sub> NFs (horizontally aligned)/PDMS	$1.48 \pm 0.04$	–	$0.0905 \pm 0.0223$	[17]
Li- and Ta-modified (K,Na)NbO <sub>3</sub> NFs/PDMS	$2.25 \pm 0.87$	5.6	–	[46]
PVDF/(K,Na)NbO <sub>3</sub> nanorod	–	3.7	–	[47]
PVDF/10 wt% (K,Na)NbO <sub>3</sub> nanorods	–	3.4	–	[48]
PVDF/(K,Na)NbO <sub>3</sub> -based nanofibrous web	–	1.9	–	[49]
BiFeO <sub>3</sub> NFs/PVDF	$3.14 \pm 1.51$	–	$0.418 \pm 0.239$	Present work

pristine PVDF-based PENG. To investigate the long-term stability of the PENGs, the output voltage performance of the BFO-5 PENG was recorded after being stored for 4 months at atmospheric conditions (Figure 5c). The BFO-5 PENG was able to produce an average output voltage of  $2.945 \pm 1.02$  V upon finger knocking, showing very little attenuation of output voltage over time. This indicated that the fabricated PENG had a very good long-term reliable performance. Table 4 lists the performance of PENGs fabricated with different nanofiller materials. It can be noted that the PENGs devices fabricated in this work deliver a higher voltage and power output compared to others listed.

## 5. Conclusion

Preparation of anisotropic single-phase bismuth ferrite NFs (BFO PNFs) was successfully achieved through electrospinning and subsequent calcination process. Three types of flexible PENG devices were fabricated by embedding 1 wt% (BFO-1), 3 wt% (BFO-3), and 5 wt% (BFO-5) of BFO PNFs in a PVDF matrix. Functional characterization of the devices showed that the voltage and power output of the PENGs was found to increase with an increase in mass fraction of BFO PNFs embedded in the PVDF matrix. PENG with a 5 wt% of embedded BFO PNFs showed a much higher voltage output of  $3.140 \pm 1.514$  V as compared to  $0.030 \pm 0.004$  V for pristine PVDF PENG,  $0.490 \pm 0.167$  V for BFO-1, and  $1.030 \pm 0.175$  V for BFO-3 PENG. Additionally, the BFO-5 PENG yielded an average output power of  $418.65 \pm 239.42$  nW, which was considerably higher than the average power output for BFO-1 at  $35.67 \pm 14.57$  nW and BFO-3 at  $135.96 \pm 34.25$  nW. Moreover, the BFO-5 PENG showed a very high peak-to-peak voltage output of 7.6 V and overall power density of  $185 \pm 106$  nW cm<sup>-2</sup>. The flexible BFO PNFs-based PENGs fabricated in this work demonstrate high-performance functional properties with respect to voltage and power output, which showcases their potential to be used as vibrational energy harvesters for powering autonomous low power sensors and wearable electronics.

## Supporting Information

Supporting Information is available from the Wiley Online Library or from the author.

## Acknowledgements

The authors gratefully acknowledge the financial support by the European Union's Horizon 2020 research and innovation program (ITN ENHANCE) under the Marie Skłodowska-Curie grant (ID: 722496). The authors are also grateful to the University of Cologne for providing excellent infrastructure. A.Q. and R.S. thank the Alexander von Humboldt Foundation and the German Federal Ministry of Education and Research (BMBF) for the financial support.

Open access funding enabled and organized by Projekt DEAL.

## Conflict of Interest

The authors declare no conflict of interest.

## Data Availability Statement

The data that support the findings of this study are available from the corresponding author upon reasonable request.

## Keywords

BFO, electrospinning, energy harvesting, lead-free materials, perovskite oxide, piezoelectric nanogenerators

Received: October 11, 2021

Revised: November 23, 2021

Published online:

[1] N. Panwar, S. Kaushik, S. Kothari, *Renewable Sustainable Energy Rev.* **2011**, *15*, 1513.

[2] J. A. Paradiso, T. Starner, *IEEE Pervasive Comput.* **2005**, *4*, 18.

[3] T. Mori, S. Priya, *MRS Bull.* **2018**, *43*, 176.

- [4] L. Dong, X. Han, Z. Xu, A. B. Closson, Y. Liu, C. Wen, X. Liu, G. P. Escobar, M. Oglesby, M. Feldman, *Adv. Mater. Technol.* **2019**, *4*, 1800148.
- [5] S. Priya, *J. Electroceram.* **2007**, *19*, 167.
- [6] H. Liu, J. Zhong, C. Lee, S.-W. Lee, L. Lin, *Appl. Phys. Rev.* **2018**, *5*, 041306.
- [7] Y. Hu, Z. L. Wang, *Nano Energy* **2015**, *14*, 3.
- [8] D. K. Bharti, M. K. Gupta, R. Kumar, N. Sathish, A. K. Srivastava, *Nano Energy* **2020**, *73*, 104821.
- [9] X. Zhou, K. Parida, O. Halevi, Y. Liu, J. Xiong, S. Magdassi, P. S. Lee, *Nano Energy* **2020**, *72*, 104676.
- [10] K. Dong, X. Peng, Z. L. Wang, *Adv. Mater.* **2020**, *32*, 1902549.
- [11] Z. Zhao, Y. Dai, S. X. Dou, J. Liang, *Mater. Today Energy* **2021**, *20*, 100690.
- [12] I. Kim, H. Roh, J. Yu, N. Jayababu, D. Kim, *ACS Energy Lett.* **2020**, *5*, 1577.
- [13] Y. Zhang, H. Kim, Q. Wang, W. Jo, A. I. Kingon, S.-H. Kim, C. K. Jeong, *Nanoscale Adv.* **2020**, *2*, 3131.
- [14] D. Yang, Y. Qiu, Q. Jiang, Z. Guo, W. Song, J. Xu, Y. Zong, Q. Feng, X. Sun, *Appl. Phys. Lett.* **2017**, *110*, 063901.
- [15] K. Batra, N. Sinha, S. Goel, H. Yadav, A. J. Joseph, B. Kumar, *J. Alloys Compd.* **2018**, *767*, 1003.
- [16] V. Vivekananthan, A. Chandrasekhar, N. R. Alluri, Y. Purusothaman, W. J. Kim, C.-N. Kang, S.-J. Kim, *Mater. Lett.* **2019**, *249*, 73.
- [17] J. Yan, Y. G. Jeong, *ACS Appl. Mater. Interfaces* **2016**, *8*, 15700.
- [18] X. Chen, S. Xu, N. Yao, Y. Shi, *Nano Lett.* **2010**, *10*, 2133.
- [19] H. Lee, H. Kim, D. Y. Kim, Y. Seo, *ACS Omega* **2019**, *4*, 2610.
- [20] W. Wu, S. Bai, M. Yuan, Y. Qin, Z. L. Wang, T. Jing, *ACS Nano* **2012**, *6*, 6231.
- [21] L. Gu, N. Cui, L. Cheng, Q. Xu, S. Bai, M. Yuan, W. Wu, J. Liu, Y. Zhao, F. Ma, *Nano Lett.* **2013**, *13*, 91.
- [22] L. Fei, Y. Hu, X. Li, R. Song, L. Sun, H. Huang, H. Gu, H. L. Chan, Y. Wang, *ACS Appl. Mater. Interfaces* **2015**, *7*, 3665.
- [23] A. Queraltó, R. Frohnhoven, S. Mathur, A. Gómez, *Appl. Surf. Sci.* **2020**, *509*, 144760.
- [24] P. Ravindran, R. Vidya, A. Kjekshus, H. Fjellvåg, O. Eriksson, *Phys. Rev. B* **2006**, *74*, 224412.
- [25] X. Ren, H. Fan, Y. Zhao, Z. Liu, *ACS Appl. Mater. Interfaces* **2016**, *8*, 26190.
- [26] S. H. Wankhade, S. Tiwari, A. Gaur, P. Maiti, *Energy Rep.* **2020**, *6*, 358.
- [27] L. Lutterotti, *Acta Crystallogr. A* **2000**, *56*, s54.
- [28] L. Lutterotti, M. Bortolotti, *IUCr. Compcomm Newsl.* **2003**, *1*, 43.
- [29] L. Lutterotti, S. Matthies, H. Wenk, *IUCr. Newsl. CPD* **1999**, *21*, 14.
- [30] C. Himcinschi, J. Rix, C. Röder, M. Rudolph, M.-M. Yang, D. Rafaja, J. Kortus, M. Alexe, *Sci. Rep.* **2019**, *9*, 1.
- [31] M. Nadeem, W. Khan, S. Khan, S. Husain, F. Singh, A. Ansari, D. Shukla, A. Ahad, V. K. Chakradhary, M. Akhtar, *J. Mater. Sci. Mater. Electron.* **2020**, *31*, 11177.
- [32] R. Agrawal, H. D. Espinosa, *Nano Lett.* **2011**, *11*, 786.
- [33] P. Shirazi, G. Ico, C. S. Anderson, M. C. Ma, B. S. Kim, J. Nam, N. V. Myung, *Adv. Sustainable Syst.* **2017**, *1*, 1700091.
- [34] R. Gregorio, R. Capitao, *J. Mater. Sci.* **2000**, *35*, 299.
- [35] P. Martins, A. Lopes, S. -MendezLanceros, *Prog. Polym. Sci.* **2014**, *39*, 683.
- [36] L. Jin, S. Ma, W. Deng, C. Yan, T. Yang, X. Chu, G. Tian, D. Xiong, J. Lu, W. Yang, *Nano Energy* **2018**, *50*, 632.
- [37] L. Lu, W. Ding, J. Liu, B. Yang, *Nano Energy* **2020**, *78*, 105251.
- [38] G. Tian, W. Deng, Y. Gao, D. Xiong, C. Yan, X. He, T. Yang, L. Jin, X. Chu, H. Zhang, *Nano Energy* **2019**, *59*, 574.
- [39] S. Abdalla, A. Obaid, F. Al-Marzouki, *Results Phys.* **2016**, *6*, 617.
- [40] X. Cai, T. Lei, D. Sun, L. Lin, *RSC Adv.* **2017**, *7*, 15382.
- [41] Y. Bormashenko, R. Pogreb, O. Stanevsky, E. Bormashenko, *Polym. Test.* **2004**, *23*, 791.
- [42] P. K. Szewczyk, A. Gradys, S. K. Kim, L. Persano, M. Marzec, A. Krysztal, T. Busolo, A. Toncelli, D. Pisignano, A. Bernasik, *ACS Appl. Mater. Interfaces* **2020**, *12*, 13575.
- [43] Y. M. Yousry, K. Yao, X. Tan, A. M. Mohamed, Y. Wang, S. Chen, S. Ramakrishna, *ACS Appl. Mater. Interfaces* **2019**, *11*, 23503.
- [44] H. B. Kang, J. Chang, K. Koh, L. Lin, Y. S. Cho, *ACS Appl. Mater. Interfaces* **2014**, *6*, 10576.
- [45] Z. Wang, Y. Zhang, S. Yang, Y. Hu, S. Wang, H. Gu, Y. Wang, H. Chan, J. Wang, *ACS Appl. Mater. Interfaces* **2015**, *7*, 4921.
- [46] A. Ichangi, V. V. Shvartsman, D. C. Lupascu, K. Lê, M. Grosch, A. K. VermaSchmidt-, C. Bohr, A. Verma, T. Fischer, S. Mathur, *J. Eur. Ceram. Soc.* **2021**, *41*, 7662.
- [47] S. Bairagi, S. W. Ali, *Eur. Polym. J.* **2019**, *116*, 554.
- [48] S. Bairagi, S. W. Ali, *Org. Electron.* **2020**, *78*, 105547.
- [49] A. Teka, S. Bairagi, M. Shahadat, M. Joshi, S. Ahammad Ziauddin, S. Ali Wazed, *Polym. Adv. Technol.* **2018**, *29*, 2537.